Direct Dark Matter Search with the Full Data Set of XMASS-I

K. Abe[1,2] for the XMASS Collaboration

[1]*Kamioka Observatory, Institute for Cosmic Ray Research, the University of Tokyo, Higashi-Mozumi, Kamioka, Hida, Gifu 506-1205, Japan*
[2]*Kavli Institute for the Physics and Mathematics of the Universe (WPI), the University of Tokyo, Kashiwa, Chiba 277-8582, Japan*

Abstract

XMASS-I, a unique experiment, carried out the long stable observation using a single-phase, large-volume liquid xenon (LXe) detector between November 20, 2013, and February 1, 2019. The results of many rare-event searches using parts of this XMASS-I data set had been reported, including WIMP dark matter (DM) searches, dark photon, axion, axion-like particle, and double electron capture. With the 5-year-long full data set of XMASS-I, we searched WIMP DM. The total livetime of the full data set is 1590.9 days for the normal-threshold trigger ($>1\,\mathrm{keV_{ee}}$) and 768.8 days for the low-threshold trigger ($>0.5\,\mathrm{keV_{ee}}$) in the 832 kg of LXe target volume. We carried out two search analyses: a fiducial volume analysis, in which we searched for nuclear recoil in the detector's fiducial volume (97 kg of LXe), and an annual modulation analysis, in which searched signals in the total volumes (832 kg of LXe). In addition to nuclear-recoil signals, we searched for signals from the bremsstrahlung and the Migdal effect in the modulation analysis. Currently, DM searches using various methods are more important than ever; therefore, search results from the full XMASS-I data set are unique and very valuable.

Keywords: dark matter, WIMP, liquid xenon, single phase, direct search
DOI: 10.31526/LHEP.2023.355

1. INTRODUCTION

Many cosmological and astrophysical observations can be explained by the existence of dark matter (DM), a hypothetical particle [1, 2]. However, the particle properties of DM are unknown. Weakly interacting massive particles (WIMPs) are accepted DM candidates [3]. A number of WIMP DM search experiments have been carried out to observe the interaction of DM with known particles, for example, the nuclei in target materials as nuclear-recoil signals [4, 5, 6, 7, 8, 9, 10].

One of these experiments, XMASS-I [11], using a simple geometry single-phase liquid xenon (LXe) detector, lasted for more than 5 years. The minimum requirements for this type of detector are the target and surrounding photo sensors. The simplicity of this design has a large potential for upscaling low BG with a minimum detector component and a low-energy threshold with a large photo coverage.

XMASS covered a wide variety of physics targets including WIMPs [12, 13, 14, 15, 16, 17, 18, 19], dark photons, axions and axion-like-particles [20, 21, 22], double electron capture [23, 24], neutrinos [25, 26], and gravitational waves [27].

By using the nuclear-recoil and electron-recoil channels, we searched WIMP DM.

2. XMASS-I EXPERIMENT

The XMASS-I detector [11] was located underground at a depth of 2,700 m water equivalent at the Kamioka Observatory. It consisted of a water-Cherenkov outer detector (OD) and a single-phase LXe inner detector (ID). The OD was a cylindrical 10 m diameter 11 m high water tank containing ultrapure water read by 72 20-inch photomultiplier tubes (PMTs). It served as a shield against fast neutrons and external γ-rays and as an active muon veto.

The structural elements of the ID included a vacuum vessel, an LXe containment vessel, and a PMT holder made of oxygen-free high-conductivity copper. The photocathodes of the 642 low radioactivity Hamamatsu R10789 PMTs [28] covered 62.4% of the ID's inner pentakis-dodecahedral surface, which was located $\sim$40 cm from its center. The average quantum efficiency of the PMTs at the LXe scintillation wavelength ($\sim$175 nm [17]) was 30%. The LXe, contained in the active volume bounded by the copper and the photocathodes had a total mass of 832 kg.

The ID triggers had two thresholds. Throughout the entire data collection period, the normal-threshold trigger required four or more PMT hits in the ID. In addition, a low-threshold trigger requiring three PMT hits in the ID was introduced on December 8, 2015. The condition of the normal-threshold trigger was unchanged.

3. FULL XMASS-I DATA SET

The data used in this analysis were collected between November 20, 2013, and February 1, 2019. The accumulated livetimes for the normal- and low-threshold trigger data are shown in Figure 1. The data collection was interrupted on two occasions for a few weeks due to the temporary extraction of the LXe to remove any dissolved nonvolatile impurities. The first purification took place from March to April 2016 by vaporizing the LXe. The second purification took place from January to February 2017 by distillation. Otherwise, the data were collected continuously under stable detector conditions, including various calibrations. The total live time was 1590.9 days for the normal-threshold trigger data and 768.8 days for the low-threshold trigger data.

The time evolution of the event rate after each reduction step, referred to as the standard cut, before proceeding with the physics analysis is shown in Figure 2. The standard cut required that no OD trigger was associated with an event, the time elapsed since the previous ID event (dT_{pre}) was at least 10 ms, and the standard deviation of the distribution of the ID hit timing for the event was less than 100 ns. The last two requirements removed events caused by after-pulses in the PMTs

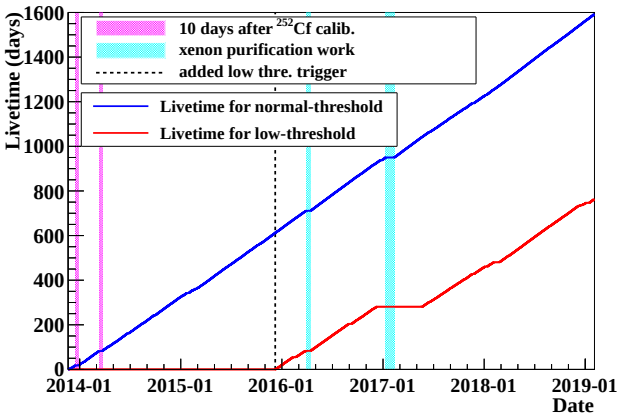

FIGURE 1: Accumulated data livetimes for the normal- (blue) and low-threshold trigger data (red). The dashed black vertical line indicates the start of the low-threshold data collection. The cyan bands indicate periods of xenon purification work. The magenta bands represent 10-day periods after detector calibration with a ^{252}Cf source.

following bright events. To remove events due to Cherenkov light emission by β-rays mainly from ^{40}K in the PMT photocathode, events in which more than 60% of the PMT hits arrived in the first 20 ns were discarded.

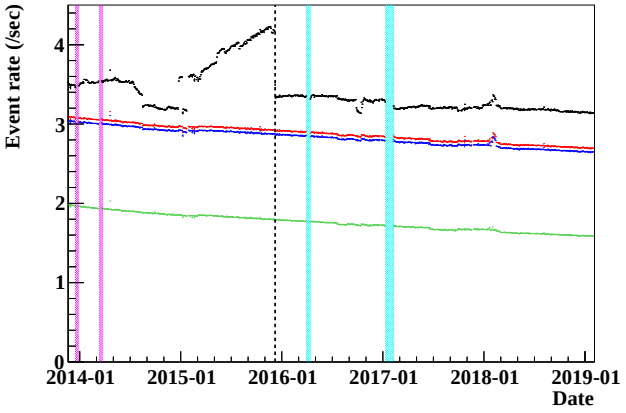

FIGURE 2: Time evolution of the event rate after each reduction step of the standard cut. From top to bottom, the event rate history after applying the requirement of having no OD trigger associated with an event (black), the time from the previous ID event (dT_{pre}) (red), the standard deviation of the ID hit timing distribution (blue), and the Cherenkov event rejection (green).

4. DETECTOR STABILITY

4.1. Pressure and Temperature

The stability of the detector temperature, measured in the LXe, and the pressure above the liquid are shown in Figure 3. The nominal temperature and pressure of the detector were -100.1°C and 0.1624 MPa, respectively. Several drops and peaks in the measurement occurred due to power outages, inner source calibrations, etc. However, even for the largest temperature drop (about 0.2 K in June 2014) due to a change of the reference temperature sensor for the feedback loop controlling the detector temperature, no impact on the PE yield was observed, as shown in the top panel of Figure 4.

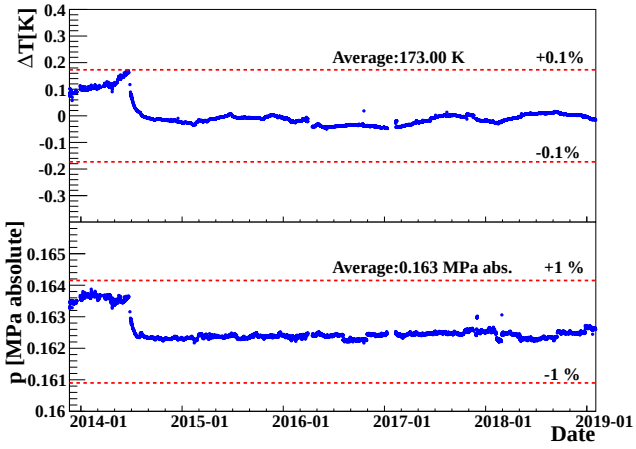

FIGURE 3: Time evolution of the detector temperature measured in the LXe and the pressure above the liquid. The temperature drop in June 2014 was due to a change of the reference temperature sensor for the refrigerator.

4.2. Light Yield and Xe Parameter

The LXe parameters, shown in Figure 4, were evaluated using calibration data taken periodically by ^{57}Co inside the detector and ^{60}Co outside. Events that led to abrupt changes were caused by a power failure in August 2014, switching to the other cold finger, and subsequent impurity removal work from December 2014 to March 2015. The absorption length for the scintillation light and the relative scintillation light yield (R_{yield}) were evaluated with the help of the detector MC simulation from the ^{57}Co calibration data.

The R_{yield} was close to constant, only varying by 1-2%. The scattering length also remained stable at around 52 cm. Variations in PE yield were explained by changes in the LXe absorption length.

4.3. PMT Status

The gain of each PMT was monitored by measuring a single PE with a blue LED embedded in the inner surface of the detector. The LED was flashed once per second, and the gain of each PMT was calculated based on the weekly averaged LED data. Figure 5 shows the time evolution of the single PE gain relative to that in the first week for each PMT. A gradual decrease in the PMT gains over the entire data-taking period was observed, and this gain evolution for each PMT was corrected when converting from the detected charge to the number of PEs.

The single rate of each PMT was also monitored by counting the number of hits in the 1 μs window before the LED flash. Figure 6 shows the time evolution of the single rate averaged over all the PMTs, the 98% coverage, and the maximum rate. The initial average single rate for each PMT was approximately

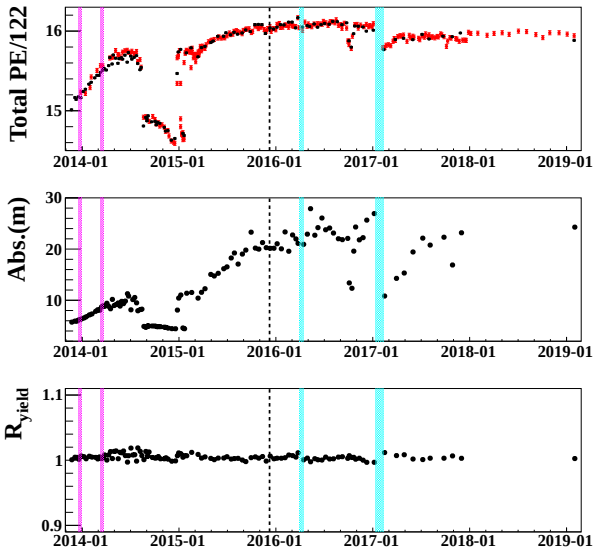

FIGURE 4: The PE yield (top panel) was monitored by 122 keV gamma rays from a ^{57}Co source (black marks), and 1177 keV and 1333 keV gamma rays from ^{60}Co were used for redundant monitoring (red marks). The middle panel shows the absorption length for the scintillation light, and the bottom panel shows the relative scintillation light yield.

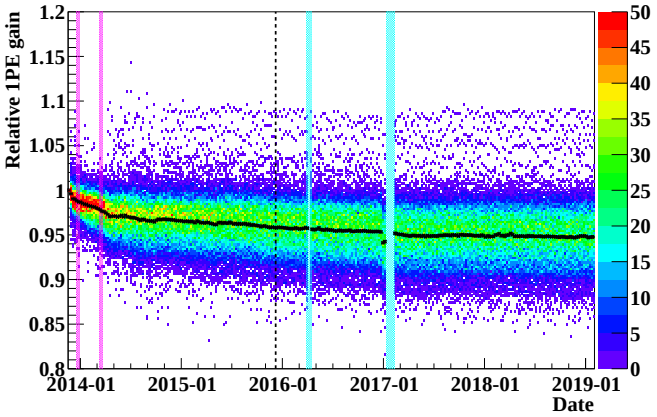

FIGURE 5: Time evolution of the single PE gain relative to that in the first week for each PMT. The black points represent the relative gain averaged over all the PMTs. This observed gain evolution for each PMT was corrected when converting from the detected charge to the number of PEs.

15 Hz, but this decreased to approximately 5 Hz during the operation. The single rate for about 10 PMTs was between several tens and several hundred Hz, and the rate for some PMTs' was unstable and occasionally increased up to a few kHz.

During the data-taking period, the number of nonoperational PMTs, referred to as dead PMTs, in the ID rose from 7 to 18, as shown in Figure 7. They were turned off mostly because the DAQ could not withstand their increased hit rate.

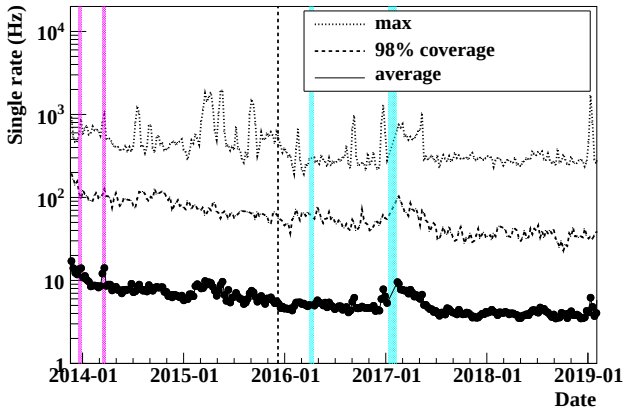

FIGURE 6: Time evolution of the single rate averaged over all the PMTs (points), the 98% coverage (dashed), and the maximum rate (dotted).

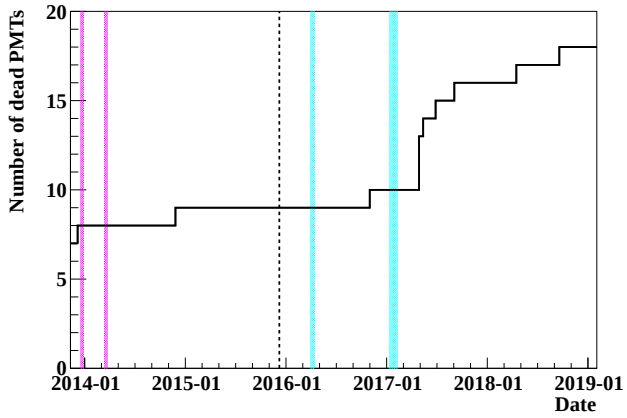

FIGURE 7: Time evolution of the number of dead PMTs in the ID.

5. ANALYSIS AND PRELIMINARY RESULTS

5.1. Modulation Analysis

The Earth's velocity relative to the distribution of DM in the galaxy changes as the Earth moves around the sun. This velocity change causes changes in the DM signal rate observed by terrestrial detectors. The size of this annual signal rate modulation, with a maximum in June, is a few percent [29]. We reported results of this modulation signal search with the XMASS-I detector, the searches for DM mass in 4–20 GeV using the nuclear recoil signal [14, 17] as well as with mass in the sub-GeV region, 0.32–1 GeV by using the bremsstrahlung effect [18].

We used all the XMASS-I observed data to search for the WIMP DM using the annual modulation, including the searches for nuclear-recoil signals, Migdal and bremsstrahlung effect signals, and Model-independent modulation.

5.2. *Nuclear-Recoil Signal Search*

The dataset for the normal-threshold trigger was divided into 125 time bins (t_{bins}), with about 15 live days in each bin. The data in each time bin were further divided into energy bins (E_{bins}), with a bin width of 0.5 $\mathrm{keV_{ee}}$. The data were fitted within an energy range from 0.5 to 20 $\mathrm{keV_{ee}}$.

Data for energy less than 1.0 $\mathrm{keV_{ee}}$ were analyzed using nuclear recoils as low as 2.3 PE (∼2.3 $\mathrm{keV_{nr}}$ and ∼0.5 $\mathrm{keV_{ee}}$) with the low-threshold trigger data. This selection of energy data improved the signal efficiency for 4 GeV and 8 GeV DM from 5% and 10% to 10% and 15%, respectively, at the lowest energy bin (2.3–4.8 $\mathrm{kev_{nr}}$).

For the modulation analysis, the WIMP signal was searched using previously written χ^2 minimization [14, 17, 18]. The observed event rate at each energy bin and time bin was compared with the expected signal using statistical and systematic errors.

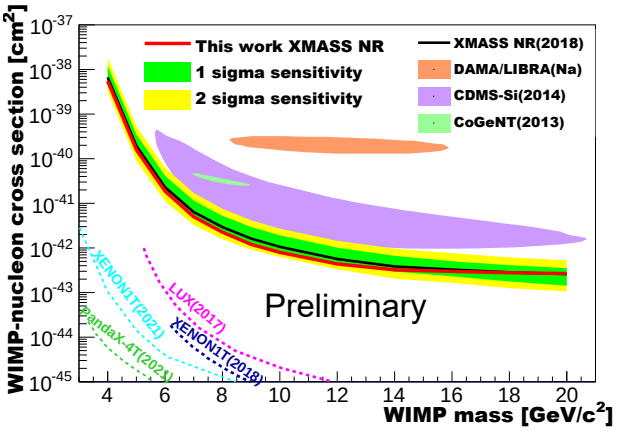

FIGURE 8: Preliminary limits on the spin-independent elastic WIMP-nucleon cross section as a function of the WIMP mass. The solid red line shows the XMASS 90% confidence-level exclusion from the annual modulation analysis. The solid black line shows the 2018 XMASS result [17]. The $\pm1\sigma$ and $\pm2\sigma$ bands represent the expected exclusion regions. Limits, as well as allowed regions from other searches based on event counting, are also shown [7, 5, 32, 33, 34, 35].

We found no significant signal; therefore, a 90% confidence level (CL) upper limit for the WIMP-nucleon cross section was set for each WIMP mass. The preliminary results are shown in Figure 8. To evaluate the sensitivity of the WIMP-nucleon cross section, we carried out a statistical test by applying the same analysis to 1,000 dummy samples using the same statistical and systematic errors as the data but without any modulation, following the procedure in [14]. The $\pm1\sigma$ and $\pm2\sigma$ bands in Figure 8 outline the expected 90% CL upper limit band for the no-modulation hypothesis using dummy samples.

5.3. *Search for the Bremsstrahlung Effect and Migdal Effect Signals*

Conventional xenon detectors should be sensitive to DM with a sub-GeV mass due to the irreducible contribution of the bremsstrahlung effect [30] and the Migdal effect [31] accompanying nuclear recoils.

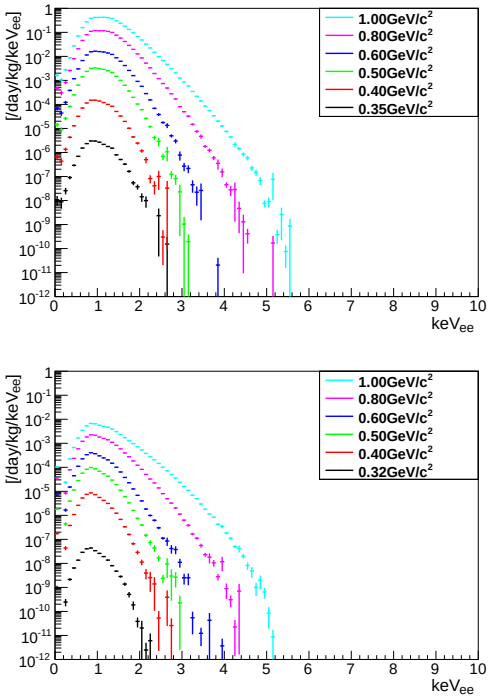

FIGURE 9: Expected signal from the Migdal (top) and bremsstrahlung effects (bottom) caused by each DM mass, with a cross section of 10^{-35} cm^2.

The bremsstrahlung effect can occur when DM collides with a nucleus, causing it to recoil and accelerate. In the case where the mass of the DM particle is 1 GeV, the energy deposited by the bremsstrahlung photon is at most 3 keV. This energy is considerably more than that deposited by elastic nuclear recoil (∼0.1 keV).

The Migdal effect at the inelastic recoil of the DM and nuclei leads to the emission of an electron from the atomic shell, which causes subsequent radiation. Although the cross sections for the bremsstrahlung (∼10^{-8} at 1 GeV) and Migdal effects (∼10^{-6} at 1 GeV) are smaller than that of the elastic nuclear recoil, because these inelastic effects lead to larger energy depositions than the elastic nuclear recoil, it is assumed that it would be possible to detect sub-GeV DM using these effects.

Figure 9 shows the expected signal from the Migdal and bremsstrahlung effects.

The energy range for both the bremsstrahlung and Migdal analyses was 1 to 20 $\mathrm{keV_{ee}}$. The threshold was set at 1 $\mathrm{keV_{ee}}$ because of a considerable increase in the uncertainty of the scintillation efficiency for electrons and gamma rays below that energy. Figure 10 shows the observed event rate with the best-fit and expected time valuation for a 0.5 GeV/c^2 WIMP signal caused by the Migdal effect at 1.0–1.5, 1.5–2.0, and 19.5–20.0 $\mathrm{keV_{ee}}$.

The results of the DM search via the Migdal and bremsstrahlung effects are shown in the sub-GeV region in Figure 11. The analysis was conducted for DM masses between 0.32 and 1 GeV/c^2 for the bremsstrahlung effect and between 0.32 and 4 GeV/c^2 for the Migdal effect. The expected sensitivity for the null-amplitude case was calculated using statistical samples.

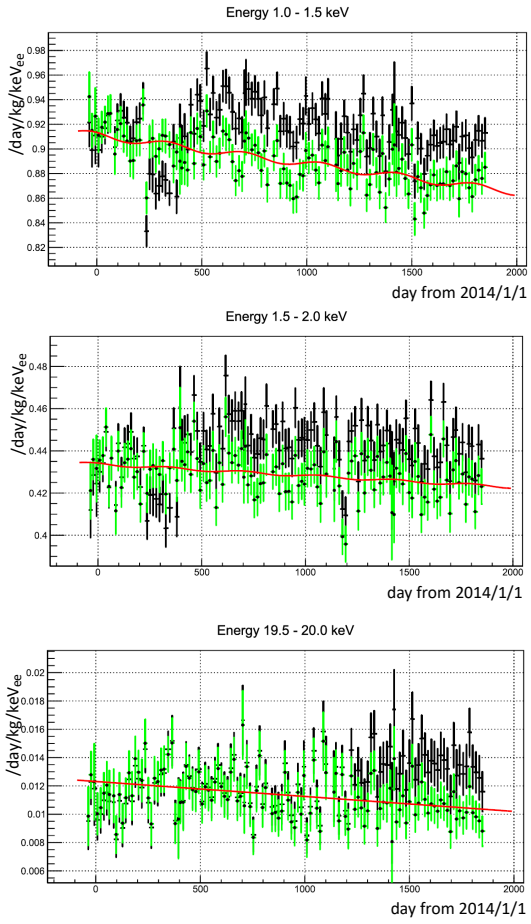

FIGURE 10: Preliminary best-fit results for data at 1.0–1.5, 1.5–2.0, and 19.5–20.0 keV$_{ee}$. The black histogram shows the data before correction, and the green histogram shows the data after correction related to the change in the absorption length [14, 17, 18] and the number of dead PMT. The red line indicates the best fit for the 0.5 GeV/c^2 WIMP spectrum caused by the Migdal effect.

5.4. Model-Independent Analysis

The model-independent analysis was also carried out with the previously written χ^2 minimization [14, 17].

We obtained the best-fit parameters in the energy region between 1 and 20 keV$_{ee}$ for the modulation hypothesis. Figure 12 shows the best-fit amplitudes as a function of energy. The $\pm1\sigma$ and $\pm2\sigma$ bands in Figure 12 represent the expected amplitude coverage derived from the dummy sample procedure described in Section 5.2. In order to test any DM model, we evaluated the positive and negative amplitude constraints separately as shown in Figure 12. As a guideline, we make direct comparisons with other experiments not by considering a specific DM model. A modulation amplitude of $\sim 2 \times 10^{-2}$ events/day/kg/keV$_{ee}$ between 1.0 and 3.5 keV$_{ee}$ was obtained by DAMA/LIBRA [39].

5.5. Fiducial Volume Analysis

As explained in [16], two different position reconstruction methods were used for the fiducial volume (FV) analysis. $R(T)$ was calculated based on the hit timings [40], and R(PE) was based on the PE distribution [11]. Events within the FV, $R(T) <$ 38 cm and R(PE) $<$ 20 cm were selected. The FV mass was 97 kg. The WIMP signal was searched for by fitting the observed energy spectrum with the sum of the evaluated BG and the signal [16].

The energy spectrum of the data and the estimated best-fit BG are presented in Figure 13. All the remaining events were consistent with our BG evaluation; therefore, a 90% CL upper

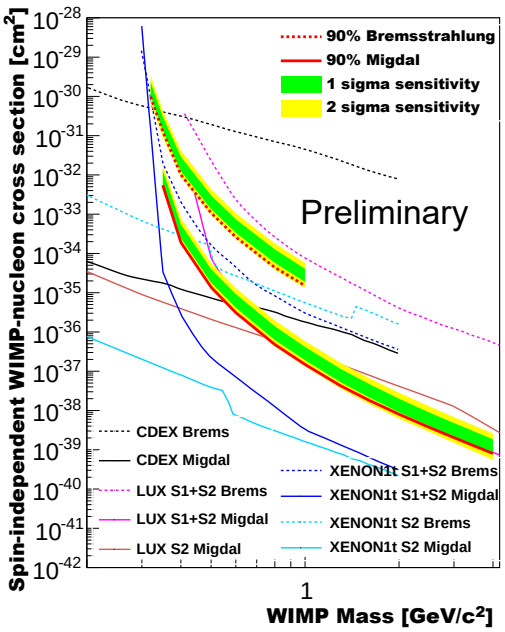

FIGURE 11: Summary of the preliminary search results of the Migdal effect analysis (solid line) and the bremsstrahlung effect analysis (dotted line) together with the limits from other experiments [6, 36, 37, 38].

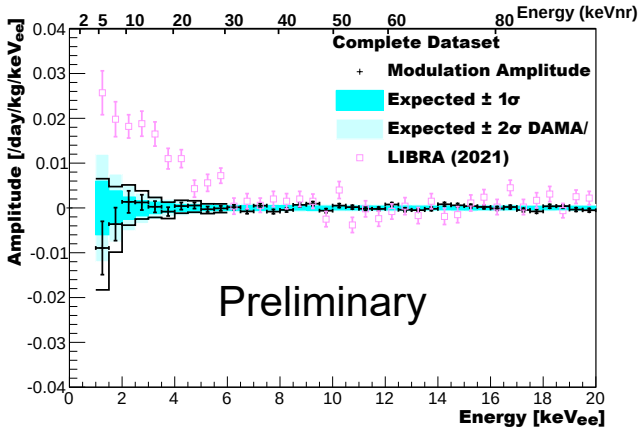

FIGURE 12: Preliminary results for the modulation amplitude as a function of energy for the model-independent analyses. The solid lines represent the 90% positive (negative) upper limits for the amplitude. The $\pm1\sigma$ and $\pm2\sigma$ bands represent the expected amplitude region. The DAMA/LIBRA result (squares) is also shown [39].

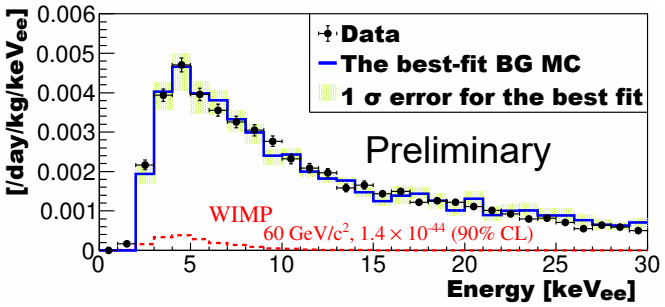

FIGURE 13: Data spectrum with the statistical error shown by the solid dots, the BG estimate shown as the blue line, and the 1σ best-fit error shown as the green shaded band. The WIMP MC expectation for 60 GeV/c^2 is shown as the red dotted line with an energy region between 2 keV$_{ee}$ and 30 keV$_{ee}$.

limit for the WIMP-nucleon cross section was calculated for each WIMP mass so that the integral of the probability density function $\exp(-\Delta\chi^2/2)$ was 90% of the total. The 90% CL upper limit for 60 GeV/c^2 WIMP is shown as the dotted line in Figure 13. The 90% CL upper limits for the different WIMP masses are plotted in Figure 14.

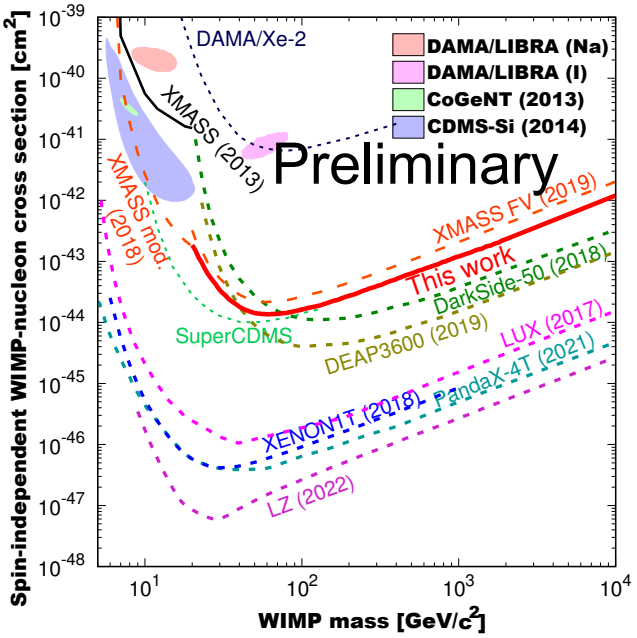

FIGURE 14: Preliminary results for the spin-independent WIMP-nucleon cross section limit as a function of the WIMP mass at the 90% CL for this work (shown as the solid red line). The experimental limits [16, 12, 17, 41, 9, 42, 10, 7, 5, 8, 4] and the allowed regions [32, 33, 34] from other studies are also shown.

6. SUMMARY

A unique, single-phase, large-volume LXe detector, XMASS-I, completed almost 5 years of stable observation between Nov. 2013 and Feb. 2019. The total live time was 1590.9 days for the normal-threshold trigger (>1 keV$_{ee}$) and 768.8 days for the low-threshold trigger (>0.5 keV$_{ee}$) for an 832 kg target volume.

WIMPs DM searches were undertaken using the full data set of XMASS-I. The preliminary results from the various analyses are shown in Figure 15 as well as improved results from our previous reports [16, 17, 18]. For the modulation analysis, the nuclear-recoil and bremsstrahlung effect signals were updated. The result of the Migdal effect signal search contributed a new addition to the analysis. The FV analysis was also updated, as a 1.5× factor improvement.

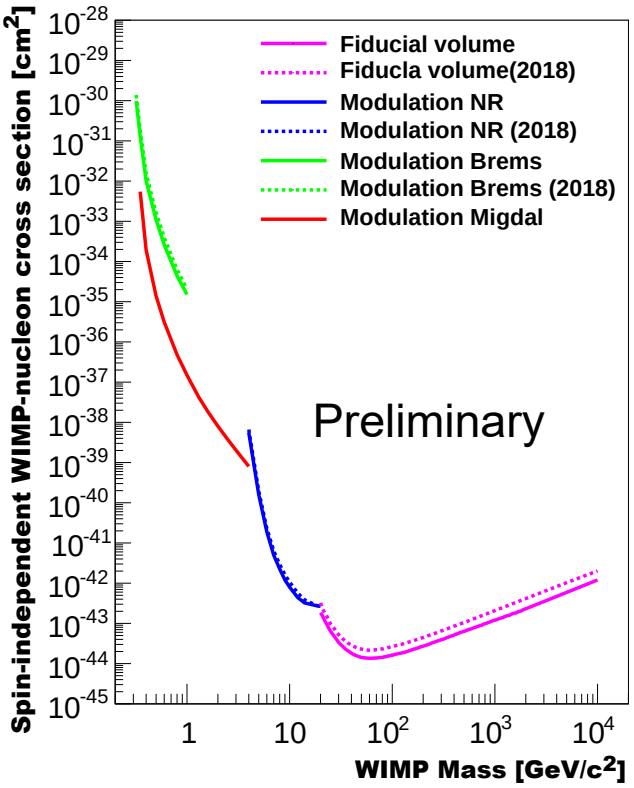

FIGURE 15: Preliminary limits obtained from the explained analyses. Solid lines are the new results, using the full XMASS-I data sets, presented in this paper, in particular the fiducial volume analysis, the multi-GeV modulation analysis via NR, and the sub-GeV modulation analysis via Migdal effect and bremsstrahlung. The dotted lines show our earlier results published in [16, 17, 18].

CONFLICTS OF INTEREST

The authors declare that there are no conflicts of interest regarding the publication of this paper.

ACKNOWLEDGMENTS

We gratefully acknowledge the cooperation of the Kamioka Mining and Smelting Company. This work was supported by the Japanese Ministry of Education, Culture, Sports, Sci-

ence and Technology, Grant-in-Aid for Scientific Research, JSPS KAKENHI Grant Nos. 19GS0204, 26104004, and 19H05805, the joint research program of the Institute for Cosmic Ray Research (ICRR), the University of Tokyo, and partially by the National Research Foundation of Korea Grant funded by the Korean Government (NRF2011-220-C00006), and the Brain Korea 21 FOUR Project grant funded by the Korean Ministry of Education.

References

[1] S. M. Faber and J. S. Gallagher, Annu. Rev. Astron. Astrophys. 17 (1979) 135.
[2] C. Patrignani et al., Particle Data Group, Chin. Phys. C 40 (2016) 010001.
[3] M. W. Goodman and E. Witten, Phys. Rev. D 31 (1985) 3059.
[4] J. Aalbers et al. (LUX-ZEPLIN (LZ) Collaboration), arXiv:hep-ex/2207.03764v2.
[5] E. Aprile et al. (XENON Collaboration), Phys. Rev. Lett. 121 (2018) 111302.
[6] E. Aprile et al. (XENON Collaboration), Phys. Rev. Lett. 123 (2019) 241803.
[7] D. S. Akerib et al. (LUX Collaboration), Phys. Rev. Lett. 118 (2017) 021303.
[8] Yue Meng et al. (PandaX-4T Collaboration), Phys. Rev. Lett. 127, 261802.
[9] P. Agnes et al. (DarkSide Collaboration), Phys. Rev. D 98, 102006 (2018).
[10] P.-A. Amaudruz et al. (DEAP-3600 Collaboration), Phys. Rev. D 100, 022004 (2019).
[11] K. Abe et al., (XMASS Collaboration), Nucl. Instr. and Meth. A716 (2013) 78.
[12] K. Abe et al. (XMASS Collaboration), Phys. Lett. B 719 (2013) 78.
[13] U. Uchida et al. (XMASS Collaboration), Prog. Theor. Exp. Phys. (2014) 063C01.
[14] K. Abe et al. (XMASS Collaboration), Phys. Lett. B 759 (2016) 272.
[15] K. Abe et al. (XMASS Collaboration), Phys Rev Lett, 113, (2014) 121301.
[16] K. Abe et al. (XMASS Collaboration), Phys. Lett. B 789 (2019) 45–53.
[17] K. Abe et al. (XMASS Collaboration), Phys. Rev. D 97, 102006 (2018).
[18] M. Kobayashi et al. (XMASS Collaboration), Phys.Lett. B 795 (2019) 308.
[19] K. Abe et al. (XMASS Collaboration), Astropart. Phys. 110 (2019) 1–7.
[20] K. Abe et al. (XMASS Collaboration), Phys.Lett. B724 (2013) 46–50.
[21] N. Oka et al. (XMASS Collaboration), Prog. Theor. Exp. Phys. 10 (2017), 103C01.
[22] K. Abe et al. (XMASS Collaboration), Phys. Lett. B787 (2018) 153–158.
[23] K. Abe et al. (XMASS Collaboration), Phys. Lett. B759 (2016) 64–68.
[24] K. Abe et al. (MASS Collaboration), Prog. Theor. Exp. Phys. 2018 (2018) 053D03.
[25] K. Abe et al. (XMASS Collaboration), Astropart. Phys. 89 (2017) 51–56.
[26] K. Abe et al. (XMASS Collaboration), Phys. Lett. B 809 (2020) 135741.
[27] K. Abe et al. (XMASS Collaboration), Astropart. Phys. 129 (2021) 102568.
[28] K. Abe et al. (XMASS Collaboration), Nucl. Instrum. and Meth. A922 (2019) 171–176.
[29] A. K. Drukier, K. Freese and D. N. Spergel, Phys. Rev. D **33** 3495 (1986).
[30] C. Kouvaris and J. Pradler, Phys. Rev. Lett. **118** (2017) 031803.
[31] M. Ibe, J. High Energ. Phys, 2018 194 (2018).
[32] J. Kopp et al., JCAP 03 (2012) 001.
[33] C. E. Aalseth et al. (CoGeNT Collaboration), Phys. Rev. D 88 (2013) 012002.
[34] R. Agnese et al. (CDMS Collaboration), Phys. Rev. Lett. 111 (2013) 251301.
[35] E. Aprile et al. (XENON Collaboration), Phys. Rev. Lett. 126, 091301 (2021).
[36] D. S. Akerib et al. (LUX Collaboration) Phys. Rev. Lett. 122, 131301.
[37] D. S. Akerib et al. (LUX Collaboration), Phys. Rev. D 104, 012011 (2021).
[38] Z. Z. Liu et al. (CDEX Collaboration), Phys. Rev. Lett. 123, 161301 (2019).
[39] R. Bernabei et al., Proceedings of Sixteenth Marcel Grossmann Meeting (2021) (World Scientific).
[40] A. Takeda for the XMASS Collaboration, Proceedings of 34th International Cosmic Ray Conference, PoS (ICRC2015) 1222.
[41] R. Bernabei et al., Phys. Lett. B 436, 379 (1998).
[42] R. Agnese et al. (SuperCDMS Collaboration), arXiv:1708.08869.